

# Weakly Supervised Volumetric Image Segmentation with Deformed Templates

Udaranga Wickramasinghe<sup>1</sup>, Patrick M. Jensen<sup>\*1,2</sup>, Jiancheng Yang<sup>\*1,3</sup>, Pascal Fua<sup>1</sup>  
<sup>1</sup>EPFL, Switzerland <sup>2</sup>DTU, Denmark <sup>3</sup>Shanghai Jiao Tong University, China

## Abstract

There are many approaches that use weak-supervision to train networks to segment 2D images. By contrast, existing 3D volumetric image approaches rely on full-supervision of a subset of 2D slices of the 3D image volume. In this paper, we propose an approach for 3D volumetric image segmentation that is truly weakly-supervised in the sense that we only need to provide a sparse set of 3D points on the surface of target objects, an easy task that can be done quickly. We use the 3D points to deform a 3D template so that it roughly matches the target object outlines and we introduce an architecture that exploits the supervision provided by the coarse template to train a network to find accurate boundaries.

We evaluate the performance of our approach on Computed Tomography (CT), Magnetic Resonance Imagery (MRI) and Electron Microscopy (EM) image datasets. We show that it outperforms the currently standard approach to weak-supervision in 3D at a much reduced supervision cost.

## 1. Introduction

State-of-the-Art volumetric segmentation techniques rely on Convolutional Neural Networks (CNNs) operating on image volumes [9, 32, 38]. However, their performance depends critically on obtaining enough annotated data, which itself requires expert knowledge and is both tedious and expensive.

Weakly-supervised image segmentation techniques can be used to mitigate this problem. They typically rely on tag annotations [14, 18, 19, 22] or coarse object annotations in the form of point annotations [3, 36, 52], bounding box annotations [21, 27, 40], scribbles [52] or approximate target shapes [26]. However, these techniques have been mostly demonstrated in 2D. For 3D volume segmentation, the dominant approach is to fully label a subset of 2D slices [9, 12]. This is referred to as *weak supervision* in the literature, even though it requires full supervision within each slice.

By contrast, we propose an approach to 3D segmentation that is truly weakly-supervised in the sense that we

only need to provide a sparse set of 3D points on the surface of the target objects, which can be done quickly and easily. To this end, we introduce the **Weak-Net** architecture depicted by Fig. 1. It comprises two U-Net-like networks. The first one is the *core network* that takes an image volume  $\mathbf{X}$  as input and produces a segmentation map  $\hat{\mathbf{Y}}$ . The second one is the *reconstruction network* that takes  $\hat{\mathbf{Y}}$  as input and outputs  $\hat{\mathbf{X}}$ , which should reproduce the original image  $\mathbf{X}$  as exactly as possible. During training, we jointly minimize the mean squared error (MSE) from  $\mathbf{X}$  to  $\hat{\mathbf{X}}$  and the binary cross entropy between  $\hat{\mathbf{Y}}$  and the mask volume  $\mathbf{Y}$  defined by the annotations. We obtain  $\mathbf{Y}$  by iteratively deforming a simple template, such as a sphere, to fit point annotations provided by an annotator, as shown in Fig. 2. The mesh is then rasterized to obtain the voxel ground truth. When the user only provides few annotations, the deformed template does not match the target object closely. Hence, minimizing the binary cross-entropy only provides coarse supervision. However, minimizing the MSE loss so that the reconstructed image resembles the original one provides the additional supervision required for good accuracy.

We evaluate the performance of **Weak-Net** on Computed Tomography (CT), Magnetic Resonance Imagery (MRI) and Electron Microscopy (EM) image datasets. We will show that it outperforms the standard approach to weak-supervision in 3D at a reduced supervision cost. More specifically, we can deliver the same accuracy as when fully annotating 2D slices for less than a third of the annotation effort. This is important because annotators typically are experts whose time is both scarce and valuable. Furthermore, it creates the basis for interactive annotating strategies that deliver the full accuracy at a lower cost than full supervision.

## 2. Related Work

We first briefly review current approaches to weak-supervision for segmentation in 2D images and 3D volumetric images. We then discuss the use of atlases for 3D segmentation in a biomedical context.

### 2.1. Weakly-Supervised Image Segmentation

**Segmenting 2D Images.** Tag annotations are among the weakest forms of annotations that have been used to seg-

\*Work done during a research visit at EPFL, Switzerland

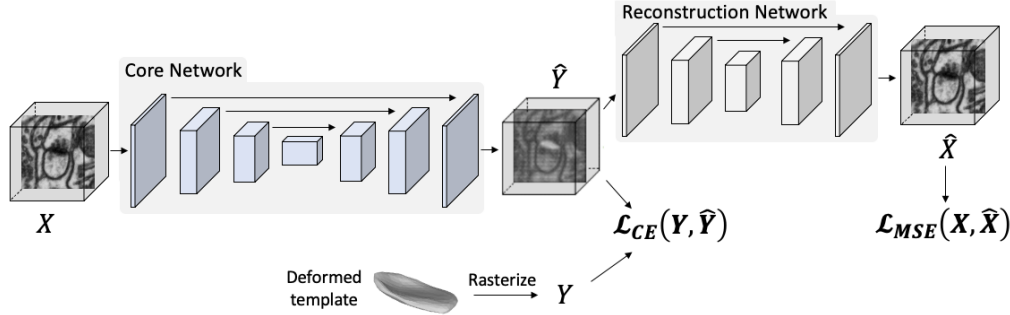


Figure 1. **Weak-Net** architecture. A first U-Net takes the image  $X$  as input and outputs a segmentation  $\hat{Y}$ , which is in turn fed to a second U-Net that outputs a reconstructed image  $\hat{X}$ . Training is achieved by jointly minimizing  $L_{mse}$  and  $L_{ce}$ . This encourages  $\hat{X}$  to resemble the original image and  $\hat{Y}$  to be similar to  $Y$ , a roughly aligned version of a template.

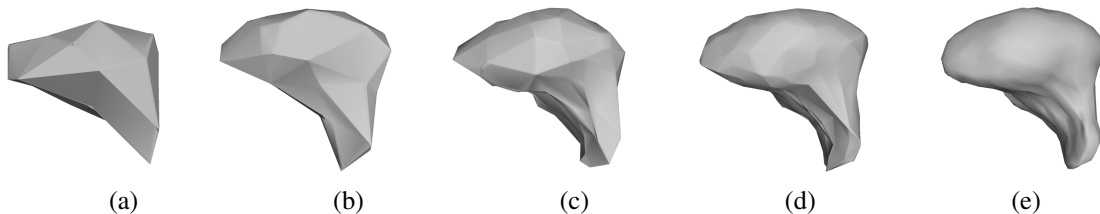


Figure 2. **Deformed templates.** (a,b,c,d,e) Deformed template using  $N = 25, 50, 125, 250,$  and  $3661$  user-supplied 3D points when segmenting a liver.  $N = 3661$  corresponds to full annotations in all slices.

ment natural images [14, 18, 19, 22] and medical images [15]. However, they rarely provide enough supervision for accurate results. Furthermore, they can only be used when segmentation can be formulated in terms of an object classification problem, which is not the case when attempting to segment a hippocampus or a liver that is present in every image. Box annotations have also been used [21, 27, 40]. In terms of localization, they are more effective than tags but still provide little information about the precise shape of the target objects. By contrast, point annotations [3, 36, 52], scribbles [52], and approximate shape annotation [26] can be used to provide useful shape information.

The annotation process can be sped-up using dynamic programming [34] or deformable contours [24], also known as *snakes*. This makes it possible to mark only a subset of points along a contour and have the system refine their location while following the target object boundary. Unfortunately, these algorithms are hard to deploy effectively in medical imagery because there are many contours besides those of interest and they can easily confuse the semi-automated algorithms, which greatly reduces their usefulness. This is addressed in [35] by introducing *deep snakes* that only need a simple approximate contour for initialization purposes. In [2, 29], the annotator is brought into the loop by giving corrective clicks when necessary, which results in an effective approach to annotation. However, these deep snakes require fully labelled data for their own training

and have only been demonstrated in the 2D case.

**Segmenting 3D Volumetric Images.** By far the most prevalent approach to weak-supervision for 3D segmentation, is to *fully* annotate subsets of slices from the training volumes [9]. Even though this reduces the segmentation effort, the annotator still has to carefully trace the object boundary in those slices. The effort can be reduced by using scribbles in individual slices [12] or any of the semi-automated techniques described above. Unfortunately, the effectiveness of those that do not require training [24, 34] is limited while the others [2, 29, 35] require full supervision and are not applicable in our scenario.

Part of the problem is that these annotation techniques operate purely in 2D without exploiting the 3D nature of the data. We will show that by so doing we only need a comparatively small number of point annotations for effective training.

## 2.2. Template Based Approaches

Shape priors have long been used for image segmentation [10, 17], well before the rise to prominence of deep networks, and more recent work use shape priors in conjunction with deep nets [33, 46] In the field of medical imaging, these priors are usually supplied in the form of sophisticated templates known as Probabilistic Atlases (PAs) that assign to each pixel or voxel a probability of belonging to a specific class. They are typically built by fusing multiple manually

annotated images and incorporated in CNN architectures as auxiliary inputs to provide localization priors that help the network find structures of interest. The PAs can be either very detailed, as in [28, 41, 42, 53], to model structures that are known in detail or very rough, as in [45], to deal with 3D structures whose shape can vary significantly.

PAs designed by point annotations have also been used in medical imaging [23, 37] as well as in natural image segmentation as a source of prior information [4, 31, 44, 50]. They are often referred to as seed layers and come in two main flavors, Gaussian priors [4, 31, 37, 44, 50] or binary seed layers [23]. These seed layers either indicate points inside the object [23, 50] or points on the boundary of the object [31, 44].

However, within the field of deep learning, PAs have been mostly used in fully-supervised approaches. An exception is the work of [42], but here they are only used for pre-training purposes.

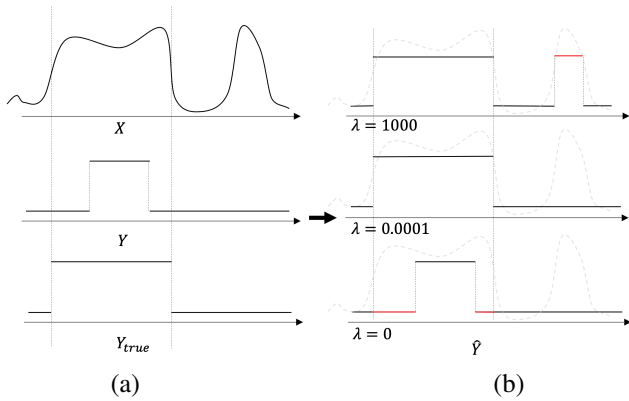


Figure 3. **Using a secondary task to improve segmentations.** (a)  $\mathbf{X}$  is the input image and  $\mathbf{Y}_{true}$  is the ground-truth segmentation.  $\mathbf{Y}$  is the atlas that is roughly correct but in which the boundaries of the target object are inaccurate. (b) When  $\lambda$  is too large,  $\mathcal{L}_{mse}$  dominates and the resulting segmentation features a spurious region shown in red that corresponds to image boundaries that are *not* those of the target structure. When  $\lambda$  is zero, only  $\mathcal{L}_{ce}$  is minimized and minimizing produces boundaries that are also those of the atlas, which are not at the right place as the denoted by the red lines. For appropriate values of  $\lambda$ , the boundaries are correct and the spurious region is eliminated.

One-shot and Few-shot learning based segmentation algorithms [11, 43, 51] can also be considered as template-based and semi-supervised approaches, as they still require at least one or a few fully annotated target objects as the atlas(es). In this work, we demonstrate another use for templates, that is, supplying rough annotations we use to train a weakly-supervised network.

## 2.3. Image Reconstruction

Image reconstruction is used for semi-supervised [8, 13, 16, 30] and unsupervised [5, 6, 49] image segmentation as an auxiliary task to improve the results. In this work, we demonstrate that this idea also applies in a weakly-supervised setting to improve the segmentations produced by the core-network trained with rough annotations. In our framework, the image reconstruction network helps refine the rough initial shapes we obtain from the annotations. There are alternative approaches to boundary refinement [1, 7, 20] but they are designed for 2D segmentation and extending them to 3D would be non-trivial.

## 3. Method

Our approach to 3D segmentation is weakly-supervised in the sense that, for training, we only need to provide a sparse set of 3D points on the surface of target objects for each image volume, which we use for training purposes. These points are used to deform a template, such as the one depicted by Fig. 2, to provide a rough indication of where the target object boundary is. It is exploited by our network to learn weights that yield accurate object boundaries. In short, we provide minimal human input at training time so that, at inference time, the trained network can be used without human intervention.

In this section, we first describe our **Weak-Net** architecture and the loss functions that allow it to effectively exploit the weak supervision provided by our rough templates. We then discuss our approach to deforming simple spherical templates given only a few user-supplied 3D points.

### 3.1. Network Architecture and Losses

Fig. 1 depicts the the **Weak-Net** architecture. It relies on two U-Net networks [9]. The first takes as input an image volume  $\mathbf{X}$  of  $D \times H \times W$ , where  $D, H, W$  stand for depth, height and width. It outputs a tensor  $\hat{\mathbf{Y}}$  of dimension  $D \times H \times W$  that stores the probabilities of each voxel belonging to the foreground. The second takes  $\hat{\mathbf{Y}}$  as input and yields  $\hat{\mathbf{X}}$ , which is of the same dimension as  $\mathbf{X}$ . Ideally,  $\hat{\mathbf{Y}}$  should be the desired segmentation and  $\hat{\mathbf{X}}$  should be equal to  $\mathbf{X}$ .

To train these two U-Nets we minimize a weighted sum of two losses

$$\begin{aligned} \mathcal{L} &= \mathcal{L}_{ce} + \lambda \mathcal{L}_{mse} , \\ \mathcal{L}_{ce} &= - \sum_{i,j,k} \mathbf{Y}_{i,j,k} \log(\hat{\mathbf{Y}}_{i,j,k}) , \\ \mathcal{L}_{mse} &= \sum_{i,j,k} \mathbf{W}_{i,j,k}^{mse} (\mathbf{X}_{i,j,k} - \hat{\mathbf{X}}_{i,j,k})^2 , \end{aligned} \quad (1)$$

where  $\mathbf{Y}$  is the rasterized template that has been fitted to the target object and  $\lambda$  is a scalar that controls the influence of the second loss.  $\mathcal{L}_{ce}$  is a standard cross entropy loss whose minimization promotes similarity between the

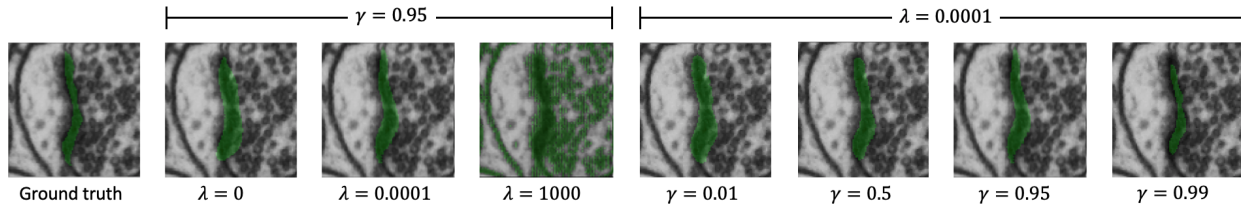


Figure 4. Impact of the  $\lambda$  parameter in the loss of Eq. 1 and the thresholding parameter  $\gamma$ . (Col. 2-4) When  $\lambda = 0$ , the segmentation is very similar to the template. When  $\lambda$  is large, there are many spurious values. (Col. 5-8) We set  $\lambda$  to  $10^{-4}$  and vary  $\gamma$ .

rasterized template  $\mathbf{Y}$  and the segmentation  $\hat{\mathbf{Y}}$ .  $\mathcal{L}_{mse}$  is a voxel-wise mean squared error in which the individual voxels are given weights  $W_{i,j,k}^{mse}$  whose value is high within a distance  $d$  from boundaries in  $\mathbf{Y}$  and low elsewhere.

In this scheme, the primary task is to minimize  $\mathcal{L}_{ce}$  to guarantee that the segmentation is roughly correct and, at inference time, we only use the first U-Net, which we will refer to as our *core network*. To obtain the final segmentation, we threshold  $\hat{\mathbf{Y}}$  using a threshold  $\gamma$ .

However, because the template can only be expected to provide a coarse depiction of the object, the  $\mathcal{L}_{ce}$  loss does not suffice on its own. To train this core network to produce accurate boundaries, we also minimize  $\mathcal{L}_{mse}$ , which serves as a secondary task. As depicted by the bottom and top rows of Fig. 3, minimizing  $\mathcal{L}_{ce}$  alone ( $\lambda=0$ ) would result in boundaries in  $\hat{\mathbf{Y}}$  that are exactly those of the template while minimizing  $\mathcal{L}_{mse}$  alone ( $\lambda=1000$ ) would produce boundaries that exist in the image but are not necessarily those we are looking for. Minimizing a properly weighted sum of the two yields segmentations that conform to the template while matching actual image boundaries, as shown in the middle row of Fig. 3 ( $\lambda=0.0001$ ).

Fig. 4 illustrates the influence of the  $\gamma$  and  $\lambda$  parameters on a real image. In practice, the results are insensitive over a wide range to how they are chosen, which we will demonstrate in the results section.

### 3.2. Template Deformation

Recall from Section 3.1, that the template  $\mathbf{Y}$  of Eq. 1 should approximately match the target structure. Hence, the annotator should supply points that are distributed across the object surface. These points can then be used to deform the template so that its boundaries roughly correspond to those of the target structure. In practice, structures of genus 0 are the most common. For these, we start from a simple spherical template but more complex ones are possible, *e.g.* those discussed in Section 2.2. We do this because creating complex atlases would require fully annotated data and it would go against the objectives of this work. As we increase the number of points, we get increasingly refined templates, as shown in Fig. 2.

To perform this deformation interactively and in real-time, we developed the GUI interface depicted by Fig. 6,

which relies on a recent approach to Active Surface Models (ASMs) [47] that makes full-use of GPUs and is therefore fast. It is implemented as an MITK [48] plugin. It lets the annotator supply a few points by clicking on 2D cross sections of the input image volume. The ASM then deforms the template, which is overlaid on the image data, both as 2D cross sections and a 3D surface rendering. The annotator can then add more points wherever the deformed template is too far from the target organ’s boundary and iterate as often as necessary. This effectively puts the human in the loop in a painless and practical way. We illustrate this in a video that can be found in the supplementary material.

## 4. Experiments

### 4.1. Datasets

In our experiments, we use three datasets acquired using different modalities to highlight the generality of our approach.

**Hippocampus Dataset** The dataset consists of 260 labeled MRI image volumes from the Medical Segmentation Decathlon [39]. The task is to segment the hippocampus and we re-sample and pad them to obtain  $64 \times 64 \times 64$  volumes. We use 130 volumes for training and the other 130 for testing. We use half of the test set as the validation set which we use for our hyper-parameter tuning and the remaining half to evaluate the final performance.

**Synaptic Junction Dataset.** We extract  $25 \times 96 \times 96 \times 96$  sub-volumes centered around a synapse from a  $500 \times 500 \times 200$  FIB-SEM image stack of a mouse cortex. We use the first 12 for training and the remaining 13 for testing, the task being to segment the synaptic cleft that separates the pre- and post-synaptic regions. In our experiments, we use the same hyper-parameters as for the hippocampus dataset.

**Liver dataset.** The dataset comprises 20 labeled CT image volumes from the CHAOS challenge [25]. The task is to segment the liver and we re-sample and pad them to obtain  $64 \times 64 \times 64$  volumes. We use 10 image volumes for training and the other 10 for testing. In our experiments, we also use the same hyper-parameters as for the hippocampus dataset.

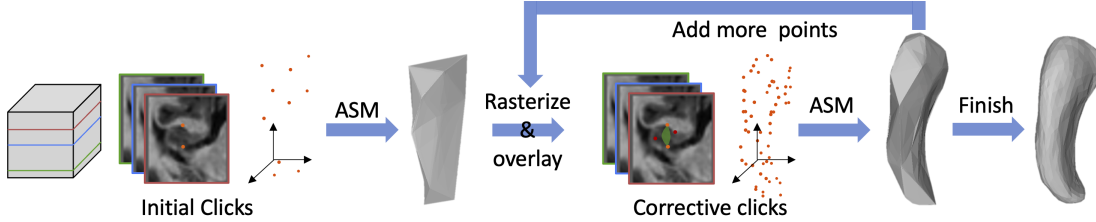


Figure 5. **Iterative annotation strategy.** The annotator provides a few 3D points, which are used to deform the template. The result is rasterized and overlaid on the images. The annotator can then add more points and deform again until the deformed template is close enough to the desired shape. For the hippocampus, shown here, this takes about 150 points to achieve 80% of the maximum accuracy that could be obtained using a fully annotated ground truth which consist of 1509 points on average.

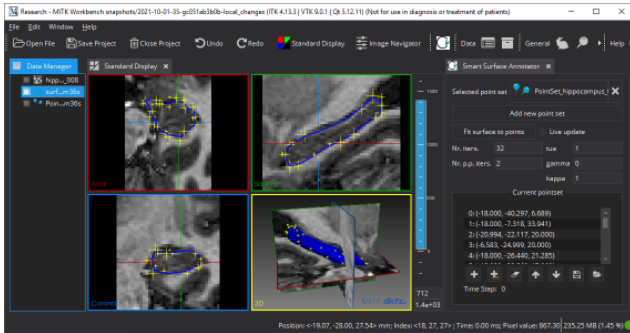


Figure 6. **Annotation GUI** A user can place points by clicking in the 2D image cross sections. A template is then deformed to fit the points and the user can place corrective clicks. The fitting takes less than one second so the process can be done interactively.

## 4.2. Metrics and Baseline

We aim to produce segmentations that are above a given quality threshold using as few annotations as possible. To formalize this goal, we use two metrics, one for quality and the other for annotation effort.

**Intersection over Union.** We use the standard IoU metric [9] to quantify segmentation quality.

**Annotation Effort.** We use the number of points provided by the annotator as a proxy for amount of effort. When the annotator provides individual points, this is clearly proportional to the time spent. When the annotator outlines contours on 2D slices, it could be argued that this overestimates the amount of effort because it is an easier task. However, in our experience it is not because precisely outlining a contour requires deliberation. The best way to do it is to use a graphics tablet and a pen, and thus requires additional hardware.

**Baseline** As discussed in Section 2.1, the generally accepted way to provide weak-supervision for 3D image segmentation is to fully annotate a small number of 2D slices [9]. To provide a baseline, we therefore use this approach to train a 3D U-Net, as described in [9]. For a fair comparison,

we use the same U-Net as in **Weak-Net**.

## 4.3. Providing Annotations

Recall from Section 3.2 that the annotator is expected to provide 3D points spread across the surface. As discussed in Section 3.2 and depicted by Fig. 5, we exploit the real-time performance of active shape models to allow the annotator to provide a few points, deform the template accordingly, and then add more points where the deformed shape is not satisfactory. In this section, we explore different approaches to supplying the annotations.

### 4.3.1 Randomized Annotations

**Setup.** To eliminate subjectivity from our experiments, we take advantage of the fact that our datasets are fully annotated to simulate this process in the following steps.

1. **Random selection.**  $N$  points are randomly selected across the 3D surface. Ideally, they should be uniformly distributed across the surface but there is no guarantee of that. To emulate the behavior of a conscientious annotator trying to achieve this, we repeat the operation  $P$  times and select the set of  $N$  points that exhibits the largest intra-point variance. As we increase  $P$ , so does the probability that the selected points will indeed be uniformly distributed. We will refer to  $P$  as the Point Spread variable.
2. **Improved selection.** We simulate the fact that a skilled annotator will provide the most informative points possible by performing  $K$  random annotations as described above, using each one to deform the template, and selecting the one that yields the highest IoU with the ground truth. As  $K$  increases, so does the probability that the deformed template will match the ground truth well. We will refer to  $K$  as the Annotator Skill variable because it reflects the annotator’s ability to select a fixed number of points to obtain the best possible result.

Hence our simulations are driven by three numbers,  $N$  the number of points per sample,  $P$  the number of samples we

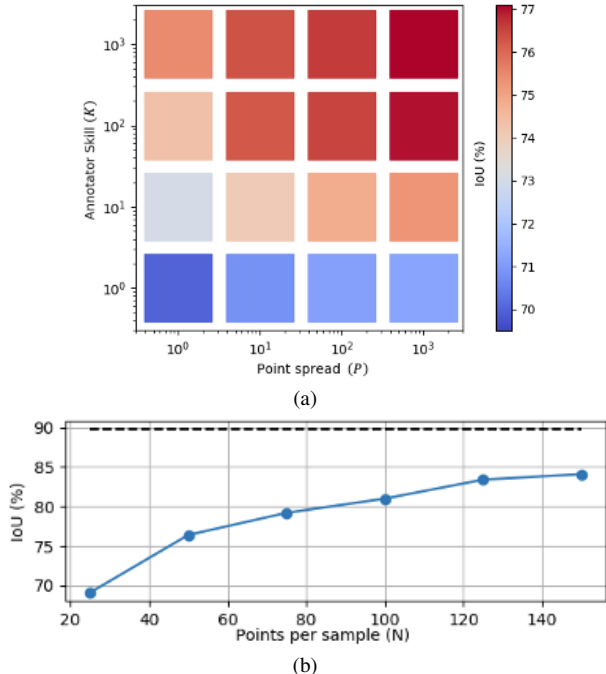


Figure 7. **Annotation simulation on the Liver dataset** (a) Reconstruction accuracy (IoU) variation for different values of  $K$  and  $P$ . (b) Reconstruction accuracy (IoU) variation as a function of the number of annotated points. The black-dashed line indicates the accuracy that would be achieved by annotating all points in each sample, that is 3661 points per sample on average for the liver dataset.

select to guarantee a good spread of the points, and  $K$  the number of attempts made to obtain a template shape that matches the ground-truth. To visualize their influence, we plot in Fig. 7(a) the average IoU in the liver dataset between the deformed template and the ground-truth as a function of  $P$  and  $K$  for a fixed value of  $N = 50$ . In Fig. 7(b), we plot the IoU as function of  $N$  for  $P = K = 100$ . Clearly, the larger  $P$ ,  $K$ , and  $N$  the higher the IoU. Interestingly, even if we use *all* the ground-truth points to deform the template, the IoU does not reach 100% because more sophisticated techniques that include sub-division of facets would be required to achieve a perfect fit. In any event, with  $P = K = 100$ , we obtain an average IoU between 80 and 90% that represent good but far from perfect fits, which is representative of what a real-life annotator might do. We will therefore use these values in our experiments.

For the baseline, we randomly pick a number of slices from three image planes to be annotated and use the ground-truth annotations for these slices. When selecting slices, we make sure the slices contain the target object.

**Comparative Results.** Given the setup described above, we now present results on the testing sets of our 3 datasets, after training with different amounts of annotations, as de-

picted by Fig. 8. When evaluating our method, we take  $P = K = 100$  and vary  $N$ , the number of annotated points per sample we provide, from 25 to 100 and  $S$  the number of samples we annotate. When evaluating the baseline, we vary the number of slices we use and the number of samples we annotate. In this case, the number of annotated points per sample is the sum of the contour lengths in every slice.

In Fig. 9(a,b), we plot the average IoUs we obtain in this manner on the hippocampus dataset as a function of the number of points per sample and the number of annotated samples. In Fig. 9(c), we plot the total annotation effort, that is the product of the number of points per sample and the number of samples, required to attain a target IoU, either 65% or 70%. As there are many ways to achieve a given IoU by increasing one number while decreasing the other, we draw *iso-IoU* curves. The baseline ones are dashed and ours are full and clearly to the left of the dashed ones. In other words, we need significantly less effort to achieve a similar result.

In Fig. 10, we report our results on the other two datasets that contain fewer samples. Hence we used all the train samples and plot the IoU as a function of the number of points per sample. For the same number of points, our approach consistently outperforms the baseline. Note also, that in the baseline method it is not possible to annotate less than one slice and therefore to reduce the annotation effort below a certain level given by the size of the contours in the annotated slice. Because we can annotate points randomly, we can actually annotate fewer, which is why the blue curves extend further to the left than the yellow ones.

### 4.3.2 Human Annotations

In practice the ground-truth will not be available and the annotations will be provided by people. We test this more realistic scenario on the Hippocampus and Liver datasets.

**Setup.** We used the GUI interface of Fig. 6 to manually annotate a subset of images using the following protocol. The annotator first supplied an initial 4 points before fitting a template and then additional ones where the fitted model seemed most distance from the target organ. As it only takes 150 to 900 ms to perform the fit, the template was updated after each new point. For the hippocampus, at most 100 points could be specified, and the liver 250. However, the annotator could stop before entering all the allowed points. To ensure errors are only caused by poor template fitting and not by annotator mistakes, the ground truth labels are overlaid on the image for visual inspection while placing the points. In the end, 2 different annotators annotated 16 hippocampus images and 5 liver images. To estimate the time for full 3D annotation, xy-slices in one Hippocampus image and one Liver image were manually delineated. For *Hippocampus*, all xy-slices were annotated. For *Liver*, 5

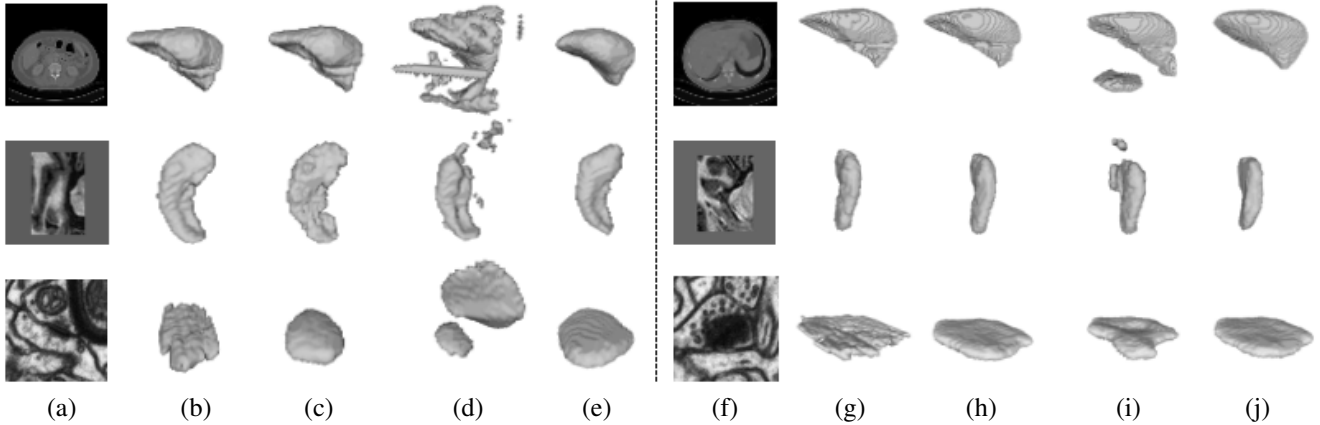


Figure 8. **Segmentation results.** (a+f) A slice from the input volume from top to bottom (b+g) Ground truth (c+h) U-Net with full-supervision (d+i) Corresponding Baseline (e) **Weak-Net** trained with 25 points per sample. (f) **Weak-Net** trained with 125 points per sample.

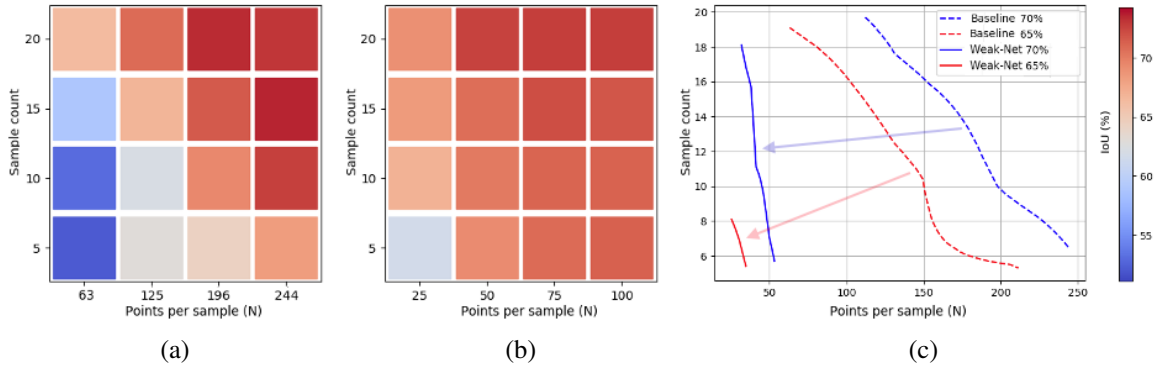


Figure 9. **Results on the hippocampus dataset.** (a) **Baseline** (b) **Weak-Net** (c) Annotation effort required to achieve 65% and 70% IoU. The blue and red arrows indicate the effort reduction our approach delivers.

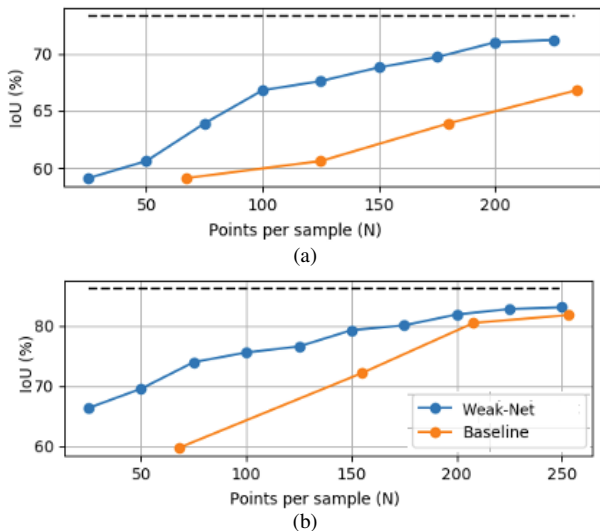


Figure 10. **IoU as function of the number of points used (N).** (a) Synaptic Junction dataset. (b) Liver dataset. The dashed line denotes fully supervised results.

evenly spaced slices were annotated and the average time was multiplied with the span of the liver along the z-axis. The annotations were performed at the original resolution of the datasets and the IoUs were also computed at this resolution.

Table 1. **Human annotation results.** Values are given as mean $\pm$ std. Times are in minutes.

		Hippocampus	Liver
Annotator 1	Max. IoU (%)	78 $\pm$ 3.0	89 $\pm$ 1.5
	Time	3.66 $\pm$ 0.60	9.17 $\pm$ 1.75
Annotator 2	Max. IoU (%)	81 $\pm$ 2.6	92 $\pm$ 0.7
	Time	5.72 $\pm$ 1.31	15.5 $\pm$ 1.47
Est. Full Annot. Time		6.65 $\pm$ 0.65	125 $\pm$ 19.3

**Comparative Results.** In Fig. 11 and Tab. 1, we report IoU as a function of the number of points supplied. The performance is roughly comparable to what we obtain with the simulated annotations of Section 4.3.1 but human-generated

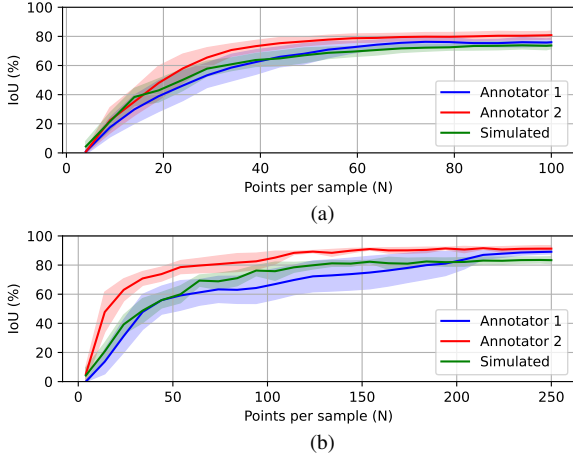


Figure 11. **Template accuracy** as a function of the number of human or simulated point annotations ( $N$ ). (a) Hippocampus. (b) Liver.

consistently deliver a higher IoU. However, in the early part of the annotation process the IoU achieved by human annotators varies significantly from dataset to dataset and annotator to annotator. Regarding time, as the Hippocampus volumes are small, point annotation is only  $\sim 1.5x$  faster than annotating the full volume. For the large Liver volumes however, point annotation is  $\sim 10x$  faster, which is significant.

#### 4.4. Limitations

It could be argued that even 25 or 50 points per sample is significant annotation effort. More sophisticated templates that are parameterized by low-dimensional latent vectors can therefore be deformed by specifying even fewer 3D points than we do now and can be developed as future work.

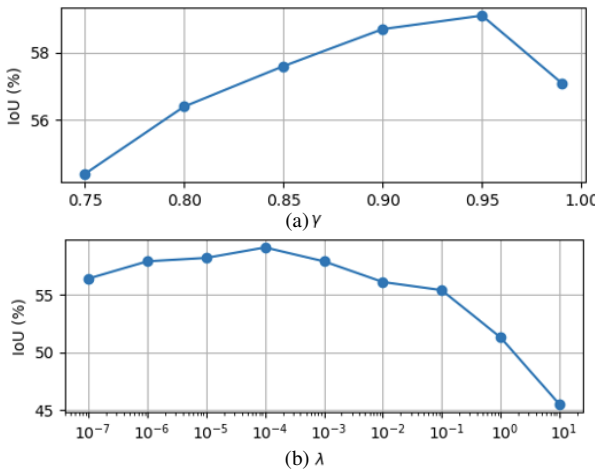


Figure 12. **Influence of  $\lambda$  and  $\gamma$** . IoU (%) as a function of  $\lambda$  in (a),  $\gamma$  in (b) on the Synaptic Junction dataset with  $N = 25$ .

Table 2. Comparative results

	Hippo.	Liver	Syn. Junction
Baseline	$71.2 \pm 0.9$	$81.2 \pm 0.8$	$68.2 \pm 0.9$
<b>Weak-Net</b>	$73.4 \pm 0.8$	$83.1 \pm 1.1$	$71.2 \pm 1.2$
Full anno.	$79.3 \pm 0.4$	$87.3 \pm 0.3$	$73.3 \pm 0.6$

## 4.5. Ablation Study

In this section, we first study the influence of the  $\lambda$  and  $\gamma$  hyper-parameters introduced in section 3 and then compare our results against those obtained using full supervision.

### 4.5.1 Impact of Hyper Parameters

We plot the variation of IoU against different values of  $\lambda$  and  $\gamma$  for the Synaptic Junction dataset. As can be seen in Fig. 12,  $\lambda$  can be chosen in the range  $10^{-6}$  to  $10^{-3}$  without any major change in performance. In practice, we used  $\lambda = 10^{-4}$  to produce the results shown Section 4 unless otherwise specified. Similarly for  $\gamma$ , we observe a peak in the range of 0.9 to 0.99. In practice, we used  $\gamma = 0.95$ .

### 4.5.2 Weak vs Full Supervision

We compare **Weak-Net** and the baseline against a U-Net trained with full supervision and report the results in Table 2. Our approach delivers 92 to 95% of the accuracy that can be achieved with full supervision with only 2 to 10% of the annotation effort for all 3 datasets.

## 5. Conclusion

We have presented a weakly supervised approach to segmenting 3D image volumes that outperforms more traditional approaches that rely on fully annotating individual 2D slices.

It relies on deforming simple spherical templates that incorporate no shape prior. In future work, to further reduce the annotation burden, we will develop more sophisticated templates that are parameterized in terms of low-dimensional latent vectors and can therefore be deformed by specifying even fewer 3D points than we do now.

## 6. Acknowledgments

This work was supported in part by a Swiss National Science Foundation grant.

## References

- [1] D. Acuna, A. Kar, and S. Fidler. Devil is in the Edges: Learning Semantic Boundaries from Noisy Annotations. In *Conference on Computer Vision and Pattern Recognition*, 2019. 3
- [2] D. Akuna, H. Ling, A. Kar, and S. Fidler. Efficient Interactive Annotation of Segmentation Datasets with Polygon-RNN++. In *Conference on Computer Vision and Pattern Recognition*, 2018. 2
- [3] A. Bearman and O. Russakovsky, V. Ferrari, and L. Fei-Fei. What’s the Point: Semantic Segmentation with Point Supervision. In *European Conference on Computer Vision*, 2016. 1, 2
- [4] G. Bertasius, H. S. Park, S. X. Yu, and J. Shi. Unsupervised Learning of Important Objects from First-Person Videos. In *International Conference on Computer Vision*, 2017. 3
- [5] A. Bielski and P. Favaro. Emergence of Object Segmentation in Perturbed Generative Models. In *Advances in Neural Information Processing Systems*, 2019. 3
- [6] M. Chen, T. Artieres, and L. Denoyer. Unsupervised Object Segmentation by Redrawing. In *Advances in Neural Information Processing Systems*, 2019. 3
- [7] X. Chen and R. Williams. Learning Active Contour Models for Medical Image Segmentation. In *Conference on Computer Vision and Pattern Recognition*, 2019. 3
- [8] S. ChenEmail, G. Bortsova, A. Juárez, G. Tulder, and M. Bruijne. Multi-Task Attention-Based Semi-Supervised Learning for Medical Image Segmentation. In *Conference on Medical Image Computing and Computer Assisted Intervention*, 2019. 3
- [9] Ö. Çiçek, A. Abdulkadir, S. Lienkamp, T. Brox, and O. Ronneberger. 3D U-Net: Learning Dense Volumetric Segmentation from Sparse Annotation. In *Conference on Medical Image Computing and Computer Assisted Intervention*, pages 424–432, 2016. 1, 2, 3, 5
- [10] D. Cremers, S. Osher, and S. Soatto. Kernel Density Estimation and Intrinsic Alignment for Shape Priors in Level-Set Segmentation. *International Journal of Computer Vision*, 2006. 2
- [11] A. Dalca, E. Yu, P. Golland, B. Fischl, M. Sabuncu, and J. Iglesias. Unsupervised Deep Learning for Bayesian Brain MRI Segmentation. In *Conference on Medical Image Computing and Computer Assisted Intervention*, 2019. 3
- [12] R. Dorent, S. Joutard, J. Shapey, S. Bisdas, N. Kitchen, R. Bradford, S. Saeed, M. Modat, S. Ourselin, and T. Vercauteren. Scribble-based Domain Adaptation via Co-segmentation. In *Conference on Medical Image Computing and Computer Assisted Intervention*, 2020. 1, 2
- [13] V. Duque, D. Chanti, M. Crouzier, A. Nordez, L. Lacourpaille, and D. Mateus. Spatio-temporal Consistency and Negative Label Transfer for 3D freehand US Segmentation. In *Conference on Medical Image Computing and Computer Assisted Intervention*, 2020. 3
- [14] T. Durand, T. Mordan, N. Thome, and M. Cord. WILDCAT: Weakly Supervised Learning of Deep Convnets for Image Classification, Pointwise Localization and Segmentation. In *Conference on Computer Vision and Pattern Recognition*, 2017. 1, 2
- [15] X. Feng, J. Yang, A. Laine, and E. Angelini. Discriminative Localization in CNNs for Weakly-Supervised Segmentation of Pulmonary Nodules. In *Conference on Medical Image Computing and Computer Assisted Intervention*, pages 568–576, 2017. 2
- [16] A. Feyjje, R. Azad, M. Pedersoli, C. Kauffman, I. Ayed, and J. Dolz. Semi-supervised few-shot learning for medical image segmentation. In *arXiv Preprint*, 2020. 3
- [17] D. Freedman and T. Zhang. Interactive Graph-Cut Based Segmentation with Shape Priors. In *Conference on Computer Vision and Pattern Recognition*, pages 755–62, 2005. 2
- [18] W. Ge, S. Yanga, and Y. Yu. Multi-Evidence Filtering and Fusion for Multi-Label Classification, Object Detection and Semantic Segmentation Based on Weakly Supervised Learning. In *Conference on Computer Vision and Pattern Recognition*, 2018. 1, 2
- [19] W. Ge, X. Lin, and Y. Yu. Weakly Supervised Complementary Parts Models for Fine-Grained Image Classification from the Bottom Up. In *Conference on Computer Vision and Pattern Recognition*, 2019. 1, 2
- [20] S. Gur, L. Wolf, L. Golgher, and P. Blinder. Unsupervised Microvascular Image Segmentation Using an Active Contours Mimicking Neural Network. In *International Conference on Computer Vision*, 2019. 3
- [21] C. Hsu, K. Hsu, C. Tsai, Y. Lin, and Y. Chuang. Weakly Supervised Instance Segmentation Using the Bounding Box Tightness Prior. In *Advances in Neural Information Processing Systems*, 2019. 1, 2
- [22] Z. Huang, X. Wang, J. Wang, W. Liu, and J. Wang. Weakly-Supervised Semantic Segmentation Network with Deep Seeded Region Growing. In *Conference on Computer Vision and Pattern Recognition*, 2018. 1, 2
- [23] M. Januszewski, J. Kornfeld, P. Li, A. Pope, T. Blakely, L. Lindsey, J. Maitin-Shepard, M. Tyka, W. Denk, and V. Jain. High-Precision Automated Reconstruction of Neurons with Flood-Filling Networks. *Nature Methods*, 2018. 3
- [24] M. Kass, A. Witkin, and D. Terzopoulos. Snakes: Active Contour Models. *International Journal of Computer Vision*, 1(4):321–331, 1988. 2

- [25] A. Kavur and M. Selver. CHAOS Challenge - Combined (CT-MR) Healthy Abdominal Organ Segmentation. In *arXiv Preprint*, 2020. 4
- [26] A. Khoreva, R. Benenson, J. Hosang, M. Hein, and B. Schiele. Simple Does It: Weakly Supervised Instance and Semantic Segmentation. In *Conference on Computer Vision and Pattern Recognition*, pages 1665–1674, 2017. 1, 2
- [27] V. Kulharia, S. Chandra, A. Agrawal, P. Torr, and A. Tyagi. Box2seg: Attention Weighted Loss and Discriminative Feature Learning for Weakly Supervised Segmentation. In *European Conference on Computer Vision*, 2020. 1, 2
- [28] M. Lee, K. Petersen, N. Pawlowski, B. Glocker, and Michiel Schaap. TETRIS: Template Transformer Networks for Image Segmentation With Shape Priors. In *IEEE Transactions on Medical Imaging*, 2019. 3
- [29] H. Ling, J. Gao, A. Kar, W. Chen, and S. Fidler. Fast Interactive Object Annotation with Curve-Gcn. In *Conference on Computer Vision and Pattern Recognition*, pages 5257–5266, 2019. 2
- [30] X. Liu, S. Thermos, A. O’Neil, and S. Tsafaris. Semi-supervised Meta-learning with Disentanglement for Domain-generalised Medical Image Segmentation. In *Conference on Medical Image Computing and Computer Assisted Intervention*, 2021. 3
- [31] K. Maninis, S. Caelles, J. Pont-Tuset, and L. Gool. Deep Extreme Cut: from Extreme Points to Object Segmentation. In *Conference on Computer Vision and Pattern Recognition*, 2018. 3
- [32] F. Milletari, N. Navab, and S.-A. Ahmadi. V-Net: Fully Convolutional Neural Networks for Volumetric Medical Image Segmentation. In *arXiv Preprint*, June 2016. 1
- [33] Z. Mirikharaji and G. Hamarneh. Star Shape Prior in Fully Convolutional Networks for Skin Lesion Segmentation. In *Conference on Medical Image Computing and Computer Assisted Intervention*, pages 737–745, 2018. 2
- [34] E.N. Mortensen and W.A. Barrett. Intelligent Scissors for Image Composition. In *ACM SIGGRAPH*, pages 191–198, August 1995. 2
- [35] S. Peng, W. Jiang, H. Pi, X. Li, H. Bao, and X. Zhou. Deep Snake for Real-Time Instance Segmentation. In *Conference on Computer Vision and Pattern Recognition*, 2020. 2
- [36] H. Qu, P. Wu, Q. Uuang, J. Yi, Z. Yan, G. Riedlinger, S. De, S. Zhang, and D. Metaxas. Weakly Supervised Deep Nuclei Segmentation Using Partial Points Annotation in Histopathology Images. In *IEEE Transactions on Medical Imaging*, 2020. 1, 2
- [37] H. Roth, L. Zhang, D. Yang, F. Milletari, Z. Xu, X. Wang, and D. Xu. Weakly supervised segmentation from extreme points. In *Conference on Medical Image Computing and Computer Assisted Intervention*, 2019. 3
- [38] A. Shvets, A. Rakhlin, A. Kalinin, and V. Iglovikov. Automatic Instrument Segmentation in Robot-Assisted Surgery Using Deep Learning. In *arXiv Preprint*, 2018. 1
- [39] Amber L Simpson, Michela Antonelli, Spyridon Bakas, Michel Bilello, Keyvan Farahani, Bram Van Ginneken, Annette Kopp-Schneider, Bennett A Landman, Geert Litjens, Bjoern Menze, et al. A Large Annotated Medical Image Dataset for the Development and Evaluation of Segmentation Algorithms. *arXiv Preprint*, 2019. 4
- [40] C. Song, Y. Huang, W. Ouyang, and L. Wang. Box-Driven Class-Wise Region Masking and Filling Rate Guided Loss for Weakly Supervised Semantic Segmentation. In *Conference on Computer Vision and Pattern Recognition*, 2019. 1, 2
- [41] H. Spitzer, K. Amunts, S. Harmeling, and T. Dickscheid. Parcellation of Visual Cortex on High-Resolution Histological Brain Sections Using Convolutional Neural Networks. In *International Symposium on Biomedical Imaging*, pages 920–923, 2017. 3
- [42] H. Spitzer, K. Kiwitz, K. Amunts, S. Harmeling, and T. Dickscheid. Improving Cytoarchitectonic Segmentation of Human Brain Areas with Self-Supervised Siamese Networks. In *Conference on Medical Image Computing and Computer Assisted Intervention*, 2018. 3
- [43] H. Tang, X. Liu, S. Sun, X. Yan, and X. Xie. Recurrent Mask Refinement for Few-Shot Medical Image Segmentation. In *International Conference on Computer Vision*, 2021. 3
- [44] Z. Wang, D. Acuna, H. Ling, A. Kar, and S. Fidler. Object Instance Annotation with Deep Extreme Level Set Evolution. In *European Conference on Computer Vision*, 2020. 3
- [45] U. Wickramasinghe, G. Knott, and P. Fua. Probabilistic atlases to enforce topological constraints. In *Conference on Medical Image Computing and Computer Assisted Intervention*, 2019. 3
- [46] U. Wickramasinghe, E. Remelli, G. Knott, and P. Fua. Voxel2mesh: 3d mesh model generation from volumetric data. In *Conference on Medical Image Computing and Computer Assisted Intervention*, 2020. 2
- [47] U. Wickramasinghe, G. Knott, and P. Fua. Deep active surface models. In *Conference on Computer Vision and Pattern Recognition*, 2021. 4
- [48] I. Wolf, M. Vetter, I. Wegner, M. Nolden, T. Bottger, M. Hastenteufel, M. Schobinger, T. Kunert, and H. Meinzer. The medical imaging interaction toolkit (MITK): a toolkit facilitating the creation of interactive software by extending VTK and ITK. In *Medical Imaging*, 2004. 4
- [49] X. Xia and B. Kulis. W-Net: A Deep Model for Fully Unsupervised Image Segmentation. In *arXiv Preprint*, 2017. 3

- [50] L. Yang, Y. Wang, X. Xiong, J. Yang, and A. Katsaggelos. Efficient Video Object Segmentation via Network Modulation. In *Conference on Computer Vision and Pattern Recognition*, 2018. 3
- [51] A. Zhao and F. Durand. Data Augmentation Using Learned Transformations for One-Shot Medical Image Segmentation. In *Conference on Computer Vision and Pattern Recognition*, 2019. 3
- [52] T. Zhao and Z. Yin. Weakly Supervised Cell Segmentation by Point Annotation. In *IEEE Transactions on Medical Imaging*, 2020. 1, 2
- [53] C. Zotti, Z. Luo, A. Lalande, and P. Jodoin. Convolutional Neural Network With Shape Prior Applied to Cardiac MRI Segmentation. In *IEEE Transactions on Medical Imaging*, 2019. 3